Eng. Sci., 2025, **35**, 1539

Engineered Science
DOI: https://dx.doi.org/10.30919/es1539

Fast-Response Ethanol Vapor Sensor Using Nickel-Doped Cerium Dioxide Nanoparticles with Enhanced Sensitivity

Yang Yang,[1,2,*] Huanxi Zhou,[2,3] Jing Huang,[2] Zicheng Zou,[1] Xiangjun Yang,[1] Tao Li,[1] Xulin Yang,[1] Kui Li[1] and Xinlu Yuan[1]

Abstract

In this paper, cerium dioxide (CeO_2) nanomaterials doped with various nickel (Ni) contents (1%, 2%, 3%, and 7% in molar ratio) were synthesized using a facile coprecipitation method. The as-prepared materials were then utilized for the sensitive detection of volatile organic compounds (VOCs), specifically ethanol. Results show that Ni doping leads to a significant improvement in ethanol response compared to the pristine CeO_2 sensor. Notably, the 2% Ni-doped CeO_2 sensor exhibits the optimal ethanol sensing performance, achieving a response value of up to ~28 to 10 ppm ethanol at operating temperature of 230 ºC. This response value is approximately 20 times higher than that of the pristine CeO_2 sensor (~1.43). Additionally, the sensor exhibits fast response time (~16 s) and recovery time (~1 s). Moreover, the 2% Ni-doped CeO_2 sensor has a response value of 3.02 for the low concentration of 0.5 ppm to ethanol vapor. This material also demonstrates great cycle stability, maintaining high stability over a 60-day testing period (RSD = 1.42%). The as-prepared Ni-doped CeO_2 sensor exhibits high response value, rapid response time and excellent cycle stability, making it a promising candidate for practical applications in ethanol sensing.

Keywords: CeO_2; Ni doped; Ethanol; Fast response; Enhanced sensitivity.
Received: 29 March 2025; Revised: 08 May 2025; Accepted: 20 May 2025.
Article type: Research article.

1. Introduction

Ethanol (CH_3CH_2OH), also known as ethyl alcohol, is a versatile solvent in chemical reactions due to its polar nature and lower boiling point compared to water.[1] Beyond industrial applications, ethanol finds widespread use in alcoholic beverages, pharmaceuticals, and cosmetic products.[2] However, despite its versatility, ethanol exposure poses significant health risks. The World Health Organization (WHO) has concluded that no level of alcohol consumption is risk-free, as ethanol is associated with the development of chronic diseases, neurotoxicity, and potential carcinogenic effects.[2] Furthermore, driving after drinking can lead to severe traffic accidents, posing a significant threat to public safety. Therefore, there is an urgent need to develop highly sensitive ethanol sensors to mitigate these risks.

In 1962, a groundbreaking study by T. Seiyama *et al.*[3] revealed a significant change in the surface resistance of metal oxide semiconductor (MOS) when exposed to gases. This finding forms the theoretical basis for the sensitivity observed in semiconductor gas sensors. Over the years, numerous research teams have dedicated efforts to the synthesis of nanostructured materials for ethanol detection. For instance, Zhang *et al.*[4] utilized a two-step hydrothermal approach to synthesize different nanostructured ZnO, the porous hollow sphere ZnO exhibited the highest gas response, achieving a response of ~51.7 to 100 ppm ethanol at 250 ºC. Similarly, Dong *et al.*[5] employed a simple hydrothermal method to fabricate Ag/SnO_2 composite, which exhibited a response of up to 60.2 for 100 ppm ethanol at 300 ºC. Additionally, Spagnoli *et al.*[6] synthesized WO_3 nanoflowers using a solvothermal method, demonstrating a response of 20.5 to 50 ppm ethanol at 250 ºC. Despite these advancements, current sensor materials still face challenges such as elevated operating temperatures and low sensitivity.

CeO_2, a versatile rare earth metal oxide semiconductor, has gained significant attention in the field of catalysis due to its unique electronic structure. This unique characteristic lends itself well to various applications in catalysis,[7] making it an

[1] *School of Mechanical Engineering, Chengdu University, Chengdu, Sichuan, 610106, China*
[2] *School of Materials Science and Engineering, Guizhou Minzu University, Guiyang, Guizhou, 550025, China*
[3] *School of Mechanical and Electrical Engineering and Architectural Engineering, Huaibei Institute of Technology, Huaibei, Anhui, 235000, China*
**Email:* yangyang823@cdu.edu.cn (Y. Yang)

invaluable material in this field. Furthermore, its exceptional redox reaction between Ce^{3+} and Ce^{4+} endows it with remarkable oxygen storage capacity,[8] providing a solid foundation for accurate and efficient detection of reducing gases. Researchers have taken advantage of this phenomenon and developed various synthesis methods to tailor the morphology and structure of CeO_2 for optimal sensing performance. Dao *et al*.[9] successfully synthesized CeO_2 nanoparticles using a solvothermal method, achieving a response of 2.3 to 100 ppm ethanol at 400 ºC. Lyu *et al*.[10] designed a core-shell hollow structured CeO_2 via a hydrothermal approach, exhibiting a response of 270% to 100 ppm acetone at 260 ºC. Similarly, Li et al.[11] synthesized CeO_2 nanorods using a solvothermal method, achieving a response of 5.32 to 1000 ppm hydrogen at 100 ºC. Despite its exceptional sensing capabilities, CeO_2 still faces challenges as a standalone sensing material.

To enhance the sensing performance of metal oxides, several strategies can be employed. On one hand, microstructures that facilitate chemical reactions can be engineered on the surface of metal oxides. On the other hand, metal doping and modification can also improve their sensing properties.[12] As a dopant, Ni^{2+} decreases the number of electrons in the antibonding state between the core metal ion and oxygen ion. This shifts the Fermi energy level downward and an increase the oxidation-reduction potential of the core metal ion during electrochemical reactions.[13] Consequently, gas adsorption is enhancd, leading to improved sensing performance. Prabhu *et al*.[14] synthesized Ni-doped ZnO nanofibres using a sol-gel electrospinning technique. The 5 w%Ni-doped ZnO nanofibres exhibited a maximum response of 132 to 50 ppm acetone vapors at 260 ºC. Meng *et al*.[15] prepared Ni-Doped Perovskite-Structured $LaFeO_3$ Nanospheres via a one-step hydrothermal method. The 2 % Ni doped $LaFeO_3$ (LFO-Ni 2%) nanospheres showed a response of 102.84 toward 100 ppm triethylamine at 190 ºC, which is 4.5 times higher than that of pristine $LaFeO_3$ (23.015). Moveover, Janene *et al*.[16] developed Ni-doped CuO/ZnO heterostructures sensor for ethanol detection. The sensitivity significantly improved after Ni doping, the 4 wt% Ni doped CuO/ZnO sensor achieving a maximum response of 97 toward 100 ppm ethanol at 225 ºC, compared to 43 for the undoped sensor at 250 ºC. Dong *et al*.[17] fabricated a 3D flower-like Ni-doped CeO_2 sensor for H_2S detection. The $Ce_{0.97}Ni_{0.03}O_{1.97}$ sensor exhibited high selectivity toward H_2S with a response of 3.1 to 500 ppb H_2S at 200 ºC, whereas pristine CeO_2 showed only 1.1 to 10 ppm H_2S at 400 ºC. These studies demonstrate that Ni doping significantly enhances the gas sensing performance due to the increase of oxygen vacancies of metal oxide semiconductors. However, few studies have explored Ni-doped CeO_2 as an ethanol gas sensor.

Herein, we present the synthesis of CeO_2 nanoparticles doped with various Ni contents (1%, 2%, 3%, and 7% in molar ratio) using a straightforward co-precipitation method. Notably, the 2% Ni-CeO_2 nanoparticles exhibit the highest response to ethanol, achieving a high response value of ~28 for 10 ppm ethanol at a working temperature of 230 ºC. Furthermore, the mechanism of ethanol response in Ni-CeO_2 has been discussed.

2. Materials and methods

2.1 Main raw materials

Cerium nitrate hexahydrate ($Ce(NO_{3)3}·6H_2O$, 99.5%) is supplied by Shanghai Aladdin Biochemical Technology Co., Ltd (China). Nickel nitrate hexahydrate ($Ni(NO_3)_2·6H_2O$, ≥98.0%) is purchased from Tianjin Damao Chemical Reagent Factory (China). Distilled water is used as the solvent, and anhydrous ethanol (AR, 99.99%) is obtained as the cleaning agent.

2.2 Preparation of Ni-doped CeO_2 nanomaterials

Ni-doped CeO_2 nanomaterials were synthesized by coprecipitation method: 13 mM (564.486 mg) of $Ce(NO_3)_3·6H_2O$ was respectively mixed with 0.13 mM (3.78 mg), 0.26 mM (7.56 mg), 0.39 mM (11.34 mg), and 0.91 mM (26.46 mg) of $Ni(NO_3)_2·6H_2O$ in 100 mL of distilled water to obtain initial solutions with different Ni molar ratios (1%, 2%, 3%, and 7%), which are ~0.67 wt%, ~1.34 wt%, ~2.01 wt%, ~4.69 wt% in weight percentages, respectively. The pristine CeO_2 was prepared as the control sample using the same procedure but without adding the Ni precursors.

Then, the initial solutions with different Ni molar ratios were added dropwise into a 300 mL beaker (the beaker was filled with 0.4 M NaOH (AR) solution in 100 mL of distilled water), and the pH of the solution was maintained at ~11 at room temperature. At this time, white precipitates were formed. The precipitates were washed several times with distilled water and ethanol, and then centrifuged at 10000 rpm for 3 times using distilled water and alcohol until the supernatant's pH reached neutral, each time for 10 min. Subsequently, the precipitates were dried at 80 °C for 3 h, and finally calcined at 400 °C in a muffle furnace for 3 h to obtain CeO_2 materials doped with Ni at a molar ratio of 1%, 2%, 3%, and 7%. The materials were stored in a desiccator for further use.

2.3 Characterizations

The morphology, elemental composition, and microstructure of the samples were characterized using a Nova Nano SEM 230 scanning electron microscope (SEM), a Tecnai G2 TF20 transmission electron microscope (TEM) equipped with an energy-dispersive spectrometer (EDX, FEI Company, USA). The phase and crystal structure of the samples were calibrated using an Empyrean X-ray diffractometer (Cu Kα, λ=0.154 nm, Panalytical Company, Netherlands) with a scanning step size of 5 °/min and a 2θ scanning range of 10°~90°. The Raman vibration characteristics were tested using a DXR2 spectrometer (Thermo Company, USA). The chemical composition of the samples was analyzed using a K-Alpha X-ray photoelectron spectrometer (Al Kα, Thermo Company,

USA) with C1s peak fixed at 284.6 eV calibrated binding energy. The specific surface area was determined by Brunauer–Emmett–Teller (V-Sorb 2800P, Gold APP Instruments Corporation China) using nitrogen adsorption–desorption. The aging of sensor samples was performed using an AS20 sensor aging station (Ailite Company, Beijing, China), and the performance of sensor samples was tested using a Chemical gas sensor-8 (CGS-8) intelligent gas sensing testing system (Beijing Ailite Technology Co., Ltd.).

2.4 Sensor preparation

A suitable amount of the synthesized sensing materials was put in a mortar and a suitable amount of anhydrous ethanol was dripped. Then, the samples were ground into a uniform paste in one direction. The paste was then uniformly brushing coated on the surface of a ceramic tube and ensuring complete coverage of the gold electrode, then dried at room temperature with the thickness of ~50 μm to obtain a by-pass type gas sensor. To ensure the stability of the gas sensor, the prepared gas sensor was aged 100 °C for 3 days before gas sensing testing.

2.5 Gas sensing measurements

The gas sensing performance was evaluated with a 20 L sealed organic glass test chamber under room environmental condition (a relative humidity of ~55% and test chamber temperature of ~21 ºC). A specific amount of target volatile organic compounds (VOCs) liquid was injected into the chamber using a micro-injector and allowed to evaporate. During the testing process, the sensor resistance reached a stable value before the test chamber was opened to expose the sensor to air. The sensor response (S) was defined as S = Ra/Rg, where Ra is the resistance in air and Rg is the resistance in the presence of the target gas. Furthermore, the response time (res) and recovery time (rec) were defined as the time required for the sensor resistance to reach 90% of its stable value after introducing or removing the target gas.

The gas concentration of the target VOCs was calculated based on the following Eq. (1), which has been widely used in the literature.[18,19]

$$V_x = \frac{V \times C \times M}{22.4 \times d \times p} \times 10^{-9} \times \frac{273+T_R}{273+T_B} \quad (1)$$

where V_x is the volume of VOCs liquid (mL), V is the volume of the test chamber (mL), M is the molecular weight of the VOCs liquid, C represents the concentration (ppm) of the evaporated gas, d is the density of the VOCs liquid, p is the purity of the VOCs liquid, T_R is the ambient temperature (ºC), T_B is the temperature in the test chamber (ºC), which can be obtained from the CGS-8 sensing testing system.

3. Results and discussion

3.1 Surface morphologies of Ni-doped CeO_2 NPs

The surface morphology of the prepared samples was observed using scanning electron microscope (SEM). It was found that both the pristine CeO_2 (without Ni doping) and 1%, 2%, 3%, and 7% Ni doped CeO_2 materials were composed of nano-particles (NPs) (Fig. S1, Supporting information), indicating that Ni doping did not affect the morphlogies of CeO_2. The Brunauer – Emmett – Teller (BET) surface areas of the prepared Ni-doped CeO_2 samples were determined using N_2 adsorption/desorption isotherms. According to the IUPAC classification,[20] all the curves exhibited type-IV isotherm behavior (Fig. S2, Supporting Information), indicating that the materials possess a mesoporous structure. Notably, the hysteresis loop varied with the Ni-doping level. Pristine CeO_2 showed a type H3 hysteresis loop, suggesting that its pore network consists primarily of macropores. In contrast, 1%, 2%, and 3% Ni-doped CeO_2 samples exhibited a type H2(a) hysteresis loop, indicative of the presence of ordered mesopores. Lastly, the 7% Ni-doped sample displayed a type H1 hysteresis loop, which is characteristic of a narrow range of uniformly sized mesopores. The estimated BET surface areas for the pristine, 1%, 2%, 3%, and 7% Ni-doped CeO_2 materials were 45.78 m^2 /g, 84.99 m^2 /g, 128.28 m^2 /g, 117.23 m^2 /g, and 90.7 m^2 /g, respectively. Among them, the 2% Ni-doped CeO_2 material had the highest specific surface area.

The nanometer particle size of CeO_2 was analyzed using transmission electron microscope (TEM) and found to range from 8-15 nm (Fig. 1a). High-resolution transmission electron microscopy (HRTEM) analysis revealed that the main crystal plane spacing of the material was 0.314 nm and 0.27 nm (Fig. 1b), which corresponds to the CeO_2 (111) and CeO_2 (200) crystal plane.[21] Selected area electron diffraction (SAED) analysis showed that the material also had other crystal planes such as (200), (220), (311), (222), (400), (331), (420), and (422) (Fig. 1c). The nanometer particle size of 2% Ni-doped CeO_2 was analyzed by TEM as well and found to range from 4-10 nm (Fig. 1d). HRTEM analysis showed that the main crystal plane spacing of the material were 0.308 nm, 0.26 nm and 0.19 nm (Fig. 1e), which correspond to the (111), (200) and (220) crystal planes of CeO_2, respectively, the smaller lattice spacing indicates Ni is embedded in the lattice of CeO_2.[22] However, SAED analysis did not reveal any Ni diffraction rings (Fig. 1f), possibly due to the low Ni doping level. Moreover, TEM-coupled energy dispersive X-ray spectroscopy (EDX) analysis has revealed that 2% Ni-doped CeO_2 is primarily composed of Ce, O, and Ni elements, whereas the undoped sample only exhibits the presence of Ce and O elements (Fig. S3, Supporting information).

3.2 Chemical structure of Ni-doped CeO_2 NPs

The phase structure and composition of the pristine CeO_2 NPs and doped with 1%, 2%, 3%, and 7% Ni were analyzed using XRD (Fig. 2a). As can be seen, nine diffraction peaks were observed at positions of 28.5º, 33.1°, 47.5°, 56.3°, 59.1°, 69.4°, 76.7°, 79.1°, and 88.4°, which were indexed to the CeO_2 crystal planes of (111), (200), (220), (311), (222), (400), (331), (420), and (422) of the fluorite crystal structure (JCPDS: 34-0394).[23] The enlarged diffraction peaks are shown in Fig. S4a

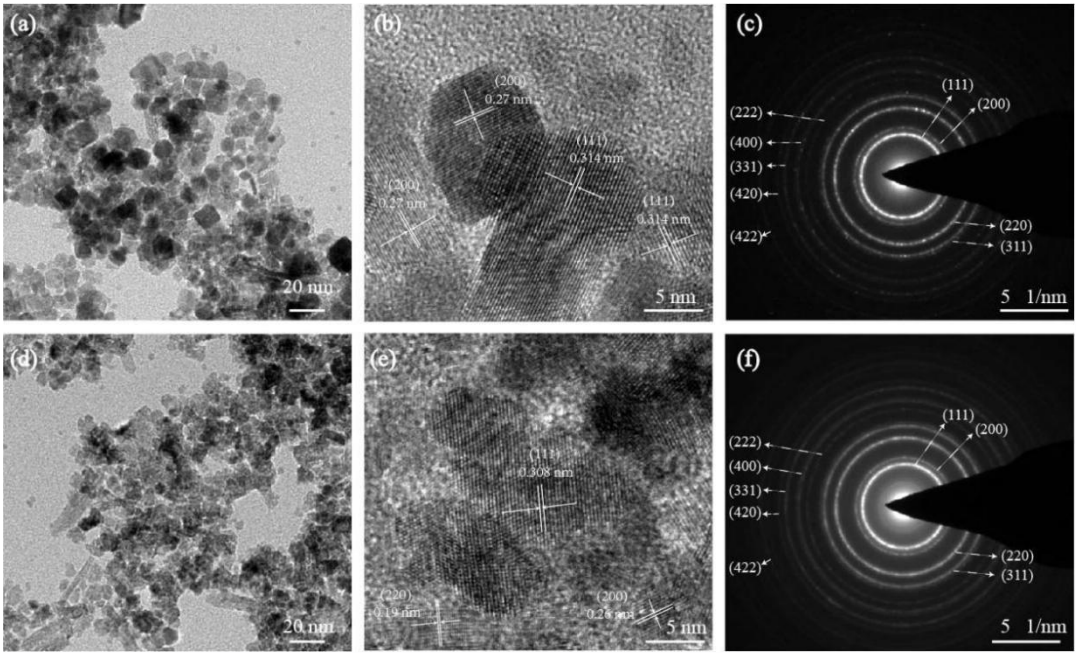

Fig. 1: (a) TEM, (b) HRTEM and (c) SEAD images for pristine CeO_2. (d) TEM, (e) HRTEM and (f) SEAD images for 2% Ni-doped CeO_2, respectively.

(Supporting information). It can be seen that the (111) peak of Ni-doped CeO_2 shifted to the right with increasing doping amount. When the doping amount was greater than 2%, the shift angle gradually decreased. This may be due to lattice contraction caused by doping ions.[24] It suggests that the CeO_2 nanometer particles doped with 2% Ni have the minimum particle size and more oxygen vacancies.[25,26]

The (111) crystal plane exhibits the peak intensity that is the most prominent across all curves, suggesting a preferential orientation for the prepared CeO_2. Nevertheless, our observations from the XRD patterns reveal an absence of any response peak pertaining to Ni, likely attributed to the comparatively low doping level of Ni. Furthermore, the doping of Ni introduces a certain degree of influence on the average grain size of CeO_2 NPs. Using the Debye–Scherrer equation,[27] the average grain sizes of the samples have been calculated in Eq. (2) and listed in Table S1 (Supporting information).

$$D = k\lambda/\beta cos\theta \quad (2)$$

where k represents a constant (taken as 0.9), D stands for the grain size, λ denotes the wavelength of X-rays (with a value of 0.154 nm), θ represents the diffraction angle, and β is the full width at half maximum (FWHM), both expressed in radians (corrected for instrument broadening).

As can be from Table S1 (Supporting information), the doping concentration of Ni increases from pristine to 2%, the average grain size of CeO_2 decreases from 10.34 nm to 6.3 nm. However, when the doping level of Ni exceeds 2%, the average grain size of CeO_2 rises slightly but remains below that of pristine CeO_2. This indicates that the doping of Ni suppresses the growth of CeO_2 grains, with the suppressive effect slightly diminishing as the doping ratio surpasses 2%.

A detailed Raman spectroscopic analysis of pristine, 1%, 2%, 3%, and 7% Ni-doped CeO_2 NPs (Fig. 2b) revealed a prominent Raman vibration peak centered at 462 cm^{-1} for all samples. This distinct peak corresponds to the symmetric stretching vibration of Ce-O in CeO_2, specifically associated with the F2g mode.[28] Notably, the Ni-doped CeO_2 NPs retained their cubic structure, and no secondary crystalline phase related to the dopant was detected in the doped samples. Additionally, the Raman spectra of pristine, 1%, 2%, 3%, and 7% Ni-doped CeO_2 NPs within the wavelength range of 440 nm to 480 nm are shown in Fig. S4b (Supporting information). When compared to pristine CeO_2 NPs, a notable shift towards lower wave numbers was observed in the Raman peak of Ni-doped CeO_2 NPs.[24] This shift is commonly attributed to the formation of oxygen vacancies within the system.[29] The incorporation of Ni ions into the CeO_2 lattice appears to suppress the F2g Raman active mode, possibly due to the doping-induced effects that promote the generation of additional oxygen vacancies.[30] Furthermore, the shift in the Raman peak can also be explained by the reduction in the size of the nanoparticles.[31]

The chemical composition and valence states of the pristine and 2% Ni-doped CeO_2 NPs were analyzed using X-ray photoelectron spectroscopy (XPS). The XPS survey spectrum reveals the elemental composition (Fig. 2c). The pristine CeO_2 NPs primarily consist of C, O, and Ce, whereas the 2% Ni-doped CeO_2 NPs contain C, O, Ni, and Ce. The presence of C is attributed to residual carbon sources encountered during sample preparation, and the C peak at 284.6 eV serves as a reference for calibrating the peak positions of the other elements (Fig. S5, Supporting information).

The Ce3d spectra of 0% and 2% Ni-doped CeO_2

nanoparticles, as shown in Fig. 2d, were split into eight distinct peaks, located at 882.7 eV (V), 885.6 eV (V1), 888.8 eV (V2), 898.4 eV (V3), 900.8 eV (U), 903.5 eV (U1), 907.8 eV (U2), and 916.7 eV (U3). Among these peaks, V, V2, V3, U, U2, and U3 represent Ce(IV)3d, with the peak at 916.5 eV (U3) being a characteristic signature of Ce(IV).[32] Conversely, V1 and U1 are indicative of Ce(III)3d. This analysis suggests that the prepared cerium oxide primarily comprises Ce(IV) with a minor contribution from Ce(III). The presence of Ce(III) suggests the existence of oxygen vacancy defects in the material.

The O1s spectra of pristine and 2% Ni-doped CeO_2 NPs are depicted in Fig. 2e. A detailed fitting analysis reveals that the peak at 529.3 eV (A) corresponds to lattice oxygen within the oxide, while the peak at 530.7 eV (B) represents vacancy oxygen in CeO_2, arising from oxygen ions present in oxygen vacancy defects. Additionally, the peak at 532.6 eV (C) is attributed to the physical adsorption of oxygen.[33] The ratio of B/A+B presented in Table S2 (Supporting information) significantly increases in the CeO_2 sample doped with 2% Ni. This observation suggests that the strong interaction between Ni-O-Ce enhances the surface oxygen density in the 2% Ni-doped CeO_2, leading to an increase in the oxygen adsorption rate.[22]

Moreover, Fig. 2f exhibits the Ni2p spectrum. The fitting analysis indicates that four peaks exist within the 850-870 eV range, specifically located at 855.45 eV, 860.65 eV, 872.9 eV, and 876.2 eV. Among these peaks, 855.45 eV and 860.65 eV correspond to the characteristic peak and satellite peak of the Ni $2p_{3/2}$ orbital, indicative of Ni(II), while 876.2 eV represents the characteristic peak and satellite peak of the Ni $2p_{1/2}$ orbital, signifying the presence of Ni(III). The XPS fitting data clearly indicates that Ni is successfully doped into the cerium oxide sample in the form of nickel oxide.[34,35] The doping concentration of Ni can be approximated by the ratio of deconvoluted peak areas, yielding an estimate of ~1.23 wt% (Table S3, Supporting information). This value is slightly lower than the initial Ni precursor addition of 1.33 wt%. This discrepancy may stem from the fact that XPS analysis probes the material to a depth of 1 to 10 nm, corresponding to a few atomic layers and a lateral extent of approximately 10 µm.[18]

3.3 Gas sensing performances of Ni-doped CeO_2 NPs

The sensing performance of MOS sensors is generally influenced by the operating temperature.[36-38] Consequently, the as prepared pristine, 1%, 2%, 3%, and 7% Ni-doped CeO_2 sensors were tested for their response to 10 ppm of ethanol gas at various operating temperatures ranging from 180 to 280 °C. The resulting response values are depicted in Fig.3a. As can be seen, the optimal working temperatures for the sensors are 250 °C, 250 °C, 230 °C, 240 °C, and 240 °C for pristine, 1%, 2%, 3%, and 7% Ni-doped CeO_2 sensors, respectively. The undoped and 1% Ni-doped CeO_2 sensors exhibit identical optimal working temperatures of 250 °C, indicating that a minimal Ni doping does not significantly alter the temperature requirement for optimal sensing. However, a significant shift is observed with 2% Ni doping, where the sensor attains both the lowest optimal operating temperature of 230 °C and the highest response value of ~28. The enhancement in gas response and the decrease in optimal operating temperature are attributed to the fact that the 2% Ni doping results in the smallest grain size, thereby maximizing the surface area. This increased surface area enhances the adsorption of oxygen species and facilitates the reaction on the surface at a lower temperature.[36] Intriguingly, as the Ni doping is further increased to 3% and 7%, the optimal operating temperature

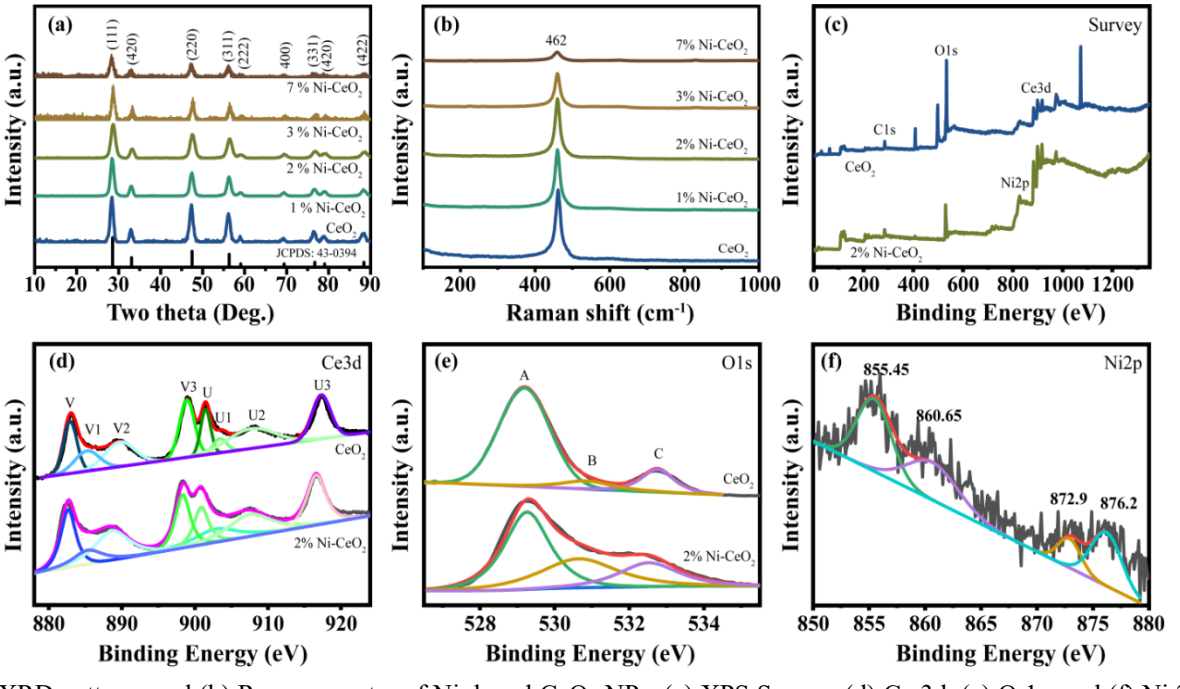

Fig. 2: (a) XRD patterns and (b) Raman spectra of Ni doped CeO_2 NPs, (c) XPS Survey, (d) Ce 3d, (e) O 1s, and (f) Ni 2p spectra for pristine and 2% Ni-doped CeO_2.

slightly increases back to 240 °C. This phenomenon can be attributed to an appropriate concentration of Ni doping initially enhances sensing performance by introducing electronic states or reactive surface sites, whereas excessive doping may introduce a high concentration of surface states, ultimately leading to a reduction in surface activity.[37]

Fig. 3b presents the response dynamics of 2% Ni-doped CeO_2 sensor towards 10 ppm ethanol gas at various operating temperatures (180 - 280 °C). The corresponding response values are shown in Fig. 3c, specifically: ~4.3, ~12, ~15.2, ~28, ~17.4, ~13, and ~10.2, respectively, which exhibit a "volcano" shape (increase-peak-decrease),[38] peaking at 230 °C with a maximum response of ~28. This phenomenon should be attributed to that the gas molecules lack sufficient thermal energy to effectively react with the adsorbed oxygen species on the sensor surface at temperatures below 230 °C. Conversely, when the operating temperature over 230 °C, the chemical adsorption of gas molecules becomes an exothermic reaction, meaning that heat is released. According to the laws of thermodynamics, this heat release opposes the forward reaction, favoring surface desorption over adsorption.[6, 38] As a consequence, the number of adsorbed gas molecules decreases, resulting in a decline in sensor response.

Seven typical reduction gases being selected and performed on the pristine and 2% Ni-doped CeO_2 sensors at same operating temperatures, including ethanol, acetone, diethyl ether, formaldehyde, isopropanol, methanol, and xylene, respectively. The real-time resistance curves are presented in logarithmic format in Fig. S6 (Supporting information), as can be seen, the initial resistance (Ra), remains consistent prior to the introduction of any gas. However, upon exposure to the reducing gas, the resistance decreases significantly and eventually stabilizes at a new value (Rg). The ratio of Ra to Rg accurately reflects the response of the sensor towards the specific gas, and the response values were depicted in Fig. 3d. It shows that the undoped CeO_2 sensor displays the low response values of ~1.43, ~1.27, ~1.16, ~1.19, ~1.1, ~1.23, and ~1.05 towards those gases, respectively. However, the 2% Ni-doped CeO_2 sensor demonstrates significantly higher responses, registering values of ~28, ~16.5, ~12.2, ~11, ~10.3, ~8.8, and ~4.2 for the same gases. This indicates that the Ni doping enhanced the sensing performance, especially towards ethanol.

The response dynamic curves of pristine, 1%, 2%, 3%, and 7% Ni-doped CeO_2 sensors towards ethanol in a gas concentrations range from 10 to 100 ppm are shown in Fig. 4a. The sensors were operated at their optimal working temperature. As observed, the response values increase proportionally with the concentration. When analyzing the linearity of the responses, it is evident that the pristine CeO_2 sensor exhibit a nonlinear relationship within the concentration range of 10-100 ppm, with a regression equation of $S = 0.0125c + 1.43$, $R^2 = 0.789$ (Fig. S7, Supporting information), which is matched with the response curve

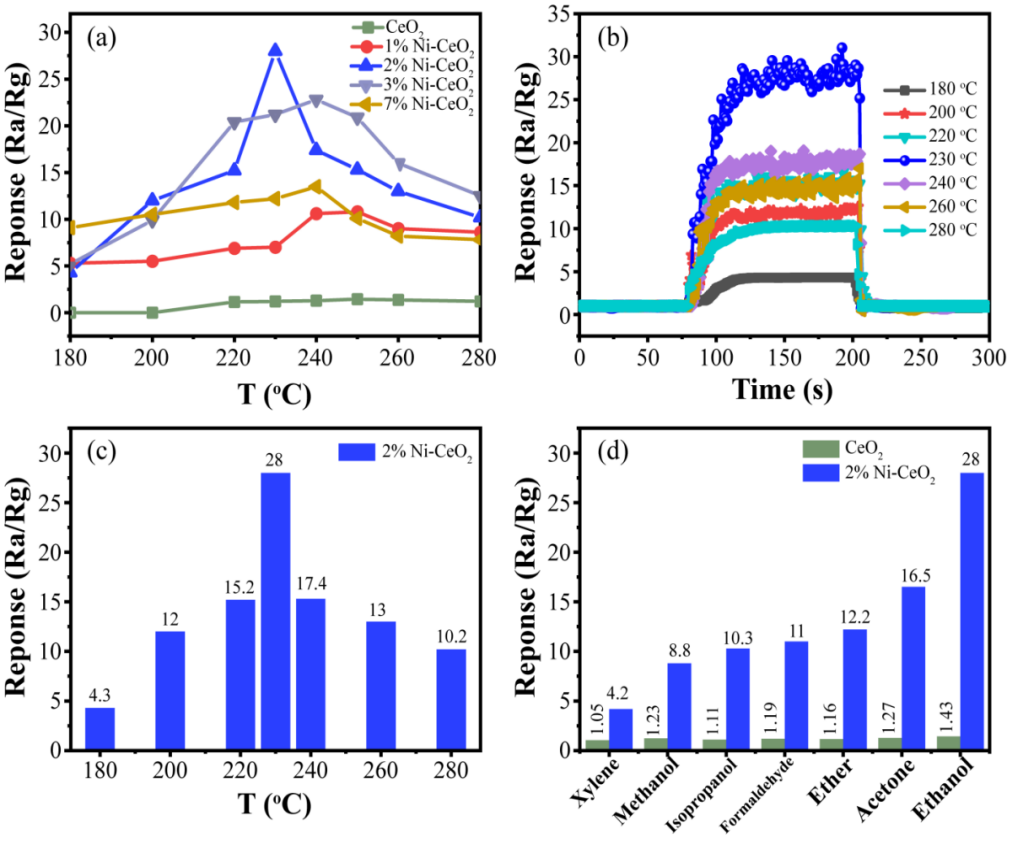

Fig. 3: (a) Response values for Ni doped CeO_2 sensors to 10 ppm ethanol at various temperatures. (b) Response dynamic curves and (c) response values of 2% Ni-doped CeO_2 sensor towards 10 ppm ethanol at different operating temperatures. (d) The response values of pristine and 2% Ni-doped CeO_2 sensors towards different gases at same operating temperatures for 10 ppm concentrations.

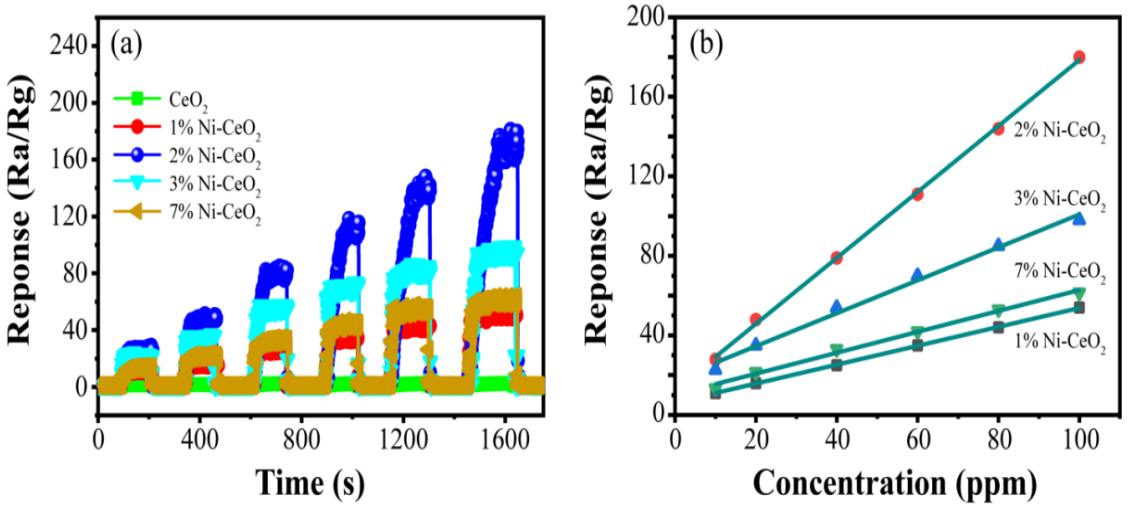

Fig. 4: (a) Gas response dynamic curves of CeO_2 doped with different concentrations of Ni towards 10-100 ppm ethanol at the optimal operating temperature. (b) Linear fitting plots of CeO_2 doped with different concentrations of Ni for 10-100 ppm ethanol at the optimal operating temperature.

presented in Fig. S8 (Supporting information). On the other hand, the response values for 1%, 2%, 3%, and 7% Ni-doped CeO_2 sensors exhibit linear relationships (Fig. 4b), with the regression equations of $S = 0.47\ c + 6.18$, $R^2 = 0.9997$; $S = 1.66c + 12.11$, $R^2 = 0.999$; $S = 0.88c + 15.25$, $R^2 = 0.9803$; $S = 0.53\ c + 10.06$, $R^2 = 0.990$, respectively.

The responses for pristine, 1%, 2%, 3%, and 7% Ni-doped CeO_2 sensors towards 10 ppm and 100 ppm ethanol concentrations were summarized in Fig. S9 (Supporting information). Notably, the response values of these sensors increase with Ni doping, peaking at 2% Ni doping for both concentrations. Specifically, for 10 ppm ethanol, the response values are ~1.43, ~11.3, ~28, ~22.3, and ~13.5 for pristine, 1%, 2%, 3%, and 7% Ni-doped CeO_2 sensors, respectively. Similarly, for 100 ppm ethanol, the corresponding response values are ~2.5, ~52, ~180, ~98, and ~62. It is noteworthy that the 2% Ni-doped CeO_2 sensor exhibits the highest response values across all concentrations studied, indicating a significant enhancement in sensing performance. In fact, its response for 100 ppm ethanol gas is approximately 72 times higher than that of the pristine CeO_2.

Furthermore, we broadened the performance of the 2% Ni-doped CeO_2 sensor operating at 230 °C in response to a low concentration of ethanol gas, specifically down to 0.5 ppm (Fig. S10, Supporting information). The sensor exhibits a significant response value of ~3.02 at a low concentration of 0.5 ppm. This result confirms the superior sensing capabilities of 2% Ni-doped CeO_2 sensor. This makes it highly promising candidates for practical applications in ethanol detection.

After exposure to the target gas, the resistance of the surface resistance-controlled sensors undergoes a decrement, eventually stabilizing at a new level. Upon subsequent removal of the ethanol gas, the resistance gradually increases, reverting back to its original state, thereby facilitating the analysis of the sensor's response and recovery duration. Fig. 5 illustrates the real-time resistance profiles of Ni-doped CeO_2 sensors with pristine, 1%, 2%, 3%, and 7% Ni content towards 10 ppm ethanol at their respective optimal operating temperatures. Additionally, Fig. S11 (Supporting Information) presents the corresponding response times and recovery times, which are derived from the response dynamics. Notably, all sensors adhere to the aforementioned resistance variation patterns in air. It is evident that the response dynamic curves correspond to the resistance dynamic curves, and the ratios of Ra and Rg are consistent with the response.

Specifically, the pristine CeO_2 sensor's response and recovery times towards 10 ppm ethanol are ~22s and ~4s, respectively. Its resistance in air measures 88 MΩ, whereas the stabilized resistance in an ethanol atmosphere is 61.53 MΩ (Fig. 5a). The 1% Ni-doped CeO_2 sensor exhibits a response time of ~20s and a recovery time of ~2s when exposed to 10 ppm ethanol. Its resistance in air is 165 MΩ, and the stable resistance in the ethanol atmosphere is 14.6 MΩ (Fig. 5b). Furthermore, the 2% Ni-doped CeO_2 sensor demonstrates the quickest response time of ~16s and the fastest recovery time of ~1s towards 10 ppm ethanol. In air, its resistance is 498 MΩ, and in the ethanol atmosphere, it stabilizes at 17.78 MΩ (Fig. 5c). The 3% Ni-doped CeO_2 sensor has a response time of ~17s and a recovery time of ~3s towards 10 ppm ethanol. In air, its resistance is 280 MΩ, and in the ethanol atmosphere, it stabilizes at 12.55 MΩ (Fig. 5d). On the other hand, the 7% Ni-doped CeO_2 sensor exhibits a response time of ~28s and a recovery time of ~3s towards 10 ppm ethanol. Its resistance in air is 180 MΩ, and the stable resistance in the ethanol atmosphere is 13.33 MΩ (Fig. 5e). Among all the tested sensors (Fig. 5f), the 2% Ni-doped CeO_2 sensor stands out with the fastest response and recovery times.

The 2% Ni-doped CeO_2 sensor demonstrates remarkable reproducibility and long-term stability when exposed to 10 ppm ethanol at 230 °C. As illustrated in Fig. 6a, the sensor undergoes five consecutive cyclic response tests, maintaining nearly identical response values throughout, which

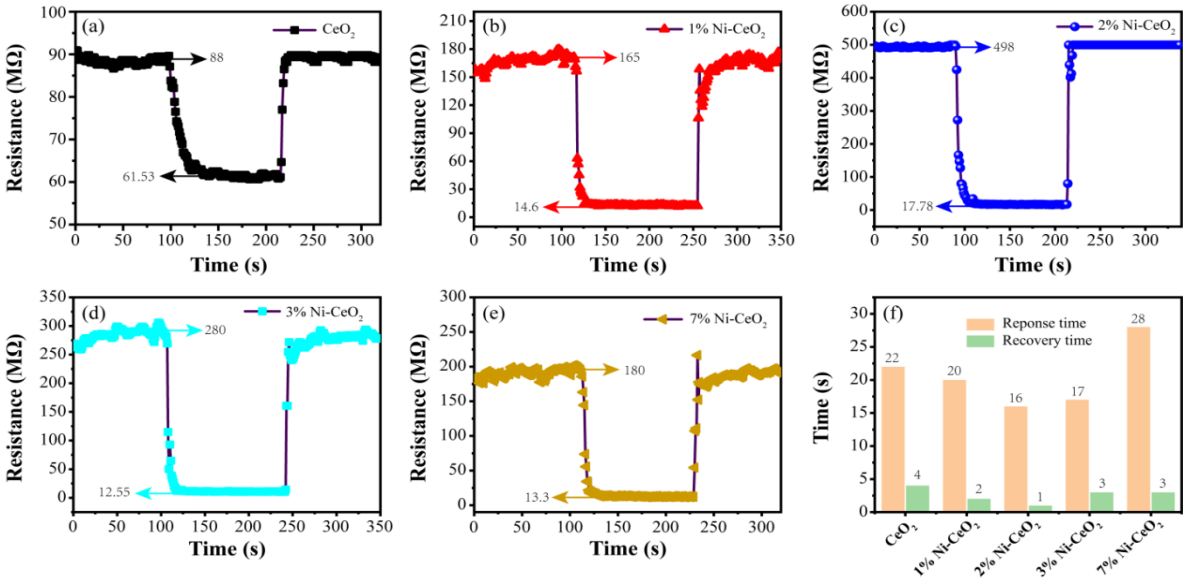

Fig. 5: Real-time resistance dynamics of Ni doped CeO_2 sensors towards 10 ppm ethanol at their optimal operating temperature: (a) pristine CeO_2, (b) 1% Ni-doped CeO_2, (c) 2% Ni-doped CeO_2, (d) 3% Ni-doped CeO_2, (e) 7% Ni-doped CeO_2. (f) Summary histogram of response and recovery times for Ni doped CeO_2 sensors towards 10 ppm ethanol.

Table 1: Comparison of the sensing performance of reported materials for ethanol.

Materials	Concentration (ppm)	Working temperature (°C)	Response (Ra/Rg)	Refs.
ZnO porous hollow sphere	100	250	51.7	[4]
Ag/SnO_2 composite	100	300	60.2	[5]
WO_3 nanosheets	50	250	20	[6]
Ceria NPs	100	400	2.3	[9]
Porous In_2O_3 Hollow Nanorods	100	200	38.6	[39]
CeO_2-decorated CdS NWs	100	160	52	[40]
CeO_2/ZnO nanosheets	100	310	86	[41]
Ni-doped CeO_2 nanoparticles	10	230	28	This work
Ni-doped CeO_2 nanoparticles	100	230	180	This work

underscores its excellent cyclic stability. Additionally, intermittent testing conducted over a span of 60 days reveals a consistent performance, with an average response value of 28.12 and a relative standard deviation (RSD) of 1.42% (Fig. 6b). This low RSD underscores the remarkable long-term stability of the 2% Ni-doped CeO_2 sensor towards ethanol gas.

A comparison with previously reported literature on sensor response values (Table 1) highlights the superior performance of the Ni-doped CeO_2 sensors developed in this study.[4-6,9,39-41] This enhanced response towards ethanol gas can be attributed to the innovative doping strategy and optimized operating conditions employed. These factors collectively contribute to the improved response of the sensor, making it a promising candidate for ethanol detection applications.

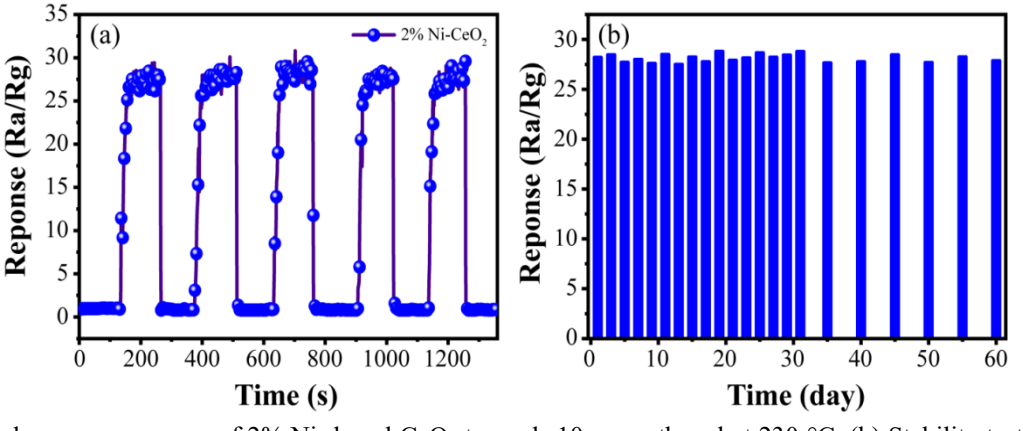

Fig. 6: (a) Five-cycle response curves of 2% Ni-doped CeO_2 towards 10 ppm ethanol at 230 °C. (b) Stability test over 60 days for 2% Ni-doped CeO_2 towards 10 ppm ethanol at 230 °C.

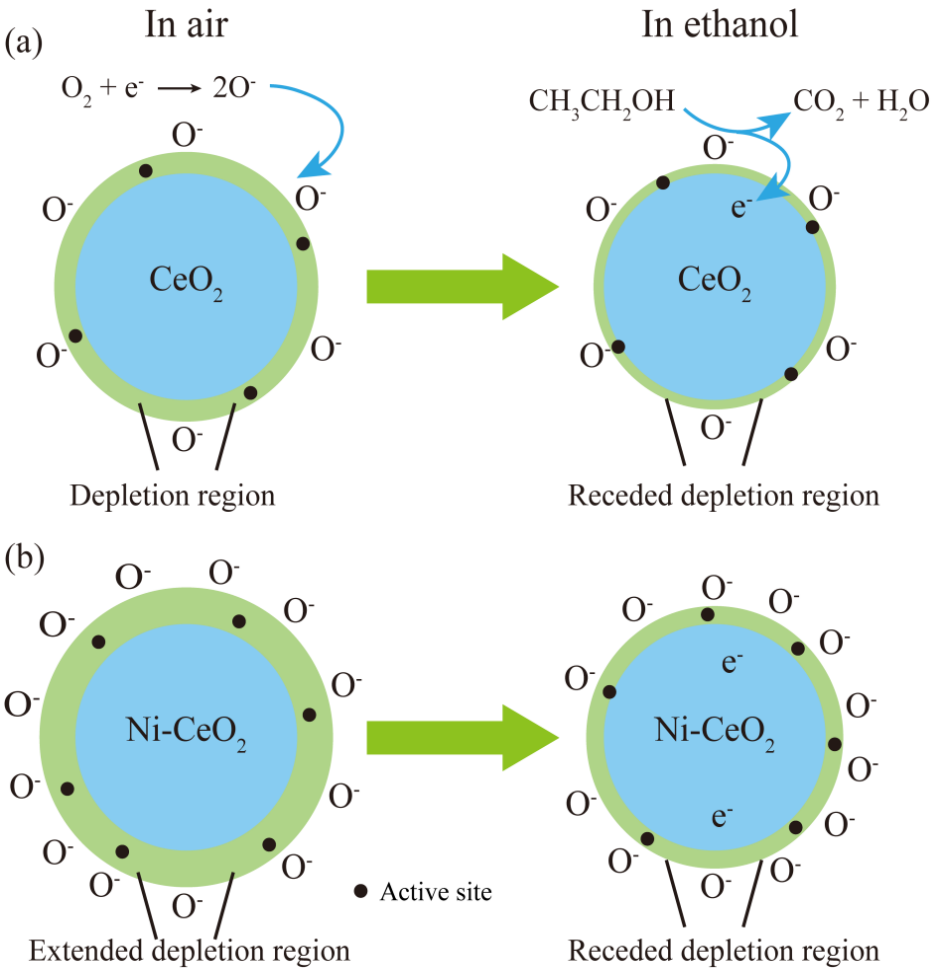

Fig. 7: Schematic illustration of the gas sensing response process (a) pristine CeO_2 and (b) Ni-doped CeO_2.

3.4 The ethanol gas sensing mechanism of Ni-doped CeO_2 NPs

The mechanism of gas sensing can be formulated based on the observation that the resistance variations observed are a direct consequence of the occurring gas-sensing reactions. When exposed to air, oxygen molecules chemically adsorb onto the surface of CeO_2 nanoparticles forming reactive oxygen species.[37] This adsorption process involves the capture of electrons from the CeO_2 material, leading to the formation of various oxygen species (O^-, O_2^-, O^{2-}) on the surface (Eqs. (5)-(8)).[4] As a result of this electron capture, an electron depletion layer is created,[37] as depicted in Fig. 7, which effectively increases the resistance of the semiconductor (Ra increases).

$$O_2(gas) \rightarrow O_2(ads) \quad (5)$$

$$O_2(ads) + e^- \rightarrow O_2^-(ads) \quad (6)$$

$$O_2^-(ads) + e^- \rightarrow 2O^-(ads) \quad (7)$$

$$O^-(ads) + e^- \rightarrow O^{2-}(ads) \quad (8)$$

When exposed to the target gas of ethanol, the ethanol molecules will absorb on the active site of CeO_2 surface (Eq. (9)), or react with the reactive surface oxygen species (Eq. (10)) [4]. This reaction releases the electrons that were previously captured, allowing them to return to the conduction band of the CeO_2 nanoparticles. This process narrows the width of the electron depletion layer and reduces the number of surface oxygen species (Fig. 7). Consequently, the resistance of the sensor decreases (Rg decreases).

$$CH_3CH_2OH(gas) \rightarrow CH_3CH_2OH\ (ads) \quad (9)$$

$$C_2H_5OH(gas) + 6O^-\ (ads) \rightarrow 2CO_2(gas) + 3H_2O(gas) + 6e^- \quad (10)$$

When Ni introduced into the CeO_2 nanoparticles, it results in profound structural and functional modifications. Firstly, the introduction of Ni leads to a refinement in the CeO_2 crystallite size, which in turn prompts an expansion of the specific surface area, which provides more sites for the adsorption and reaction of gas molecules. Therefore, the thickness of the charge depletion layer increases.[42] Secondly, Ni^{2+} ions within the CeO_2 lattice act as catalytic active sites. These sites facilitate the formation of oxygen vacancies, which play an important role in the oxygen ionosorption process and the subsequent reactions with reducing gases.[43] Thirdly, the Ni doping increases the oxygen content adsorbed on the CeO_2 surface, which promotes the formation of reactive oxygen species.[44] Therefore, a low concentration Ni doping extremely enhanced the sensing performance of CeO_2.

4. Conclusion

This paper presents the successful fabrication of CeO_2 NPs doped with varying concentrations of Ni using the coprecipitation method. A detailed analysis using scanning electron microscope (SEM) revealed that both pristine and 2% Ni-doped CeO_2 NPs exhibited a highly dispersed morphology. This observation was further corroborated by transmission electron microscopy (TEM) and X-ray photoelectron spectroscopy (XPS), confirming the successful doping of Ni. Notably, X-ray diffraction (XRD) analysis demonstrated that the 2% Ni-doped CeO_2 NPs possess a significantly smaller grain size compared to the pristine form.

In terms of gas response, 2% Ni-doped CeO_2 NPs sensor exhibits exceptional response towards ethanol gas, operating optimally at 230 °C. Remarkably, the sensor displayed a remarkably sensitive response value of ~28 towards 10 ppm ethanol, along with rapid response and recovery times of ~16 seconds and ~1 second, respectively. Furthermore, tests conducted on varying concentrations of ethanol gas revealed a robust linear relationship between the response values and concentrations, achieving a high linear fitting result of R^2=0.9977.

During a 60-day stability test, the sensor exhibited remarkable stability, with an RSD of only ~1.42% for its response to 10 ppm ethanol gas. The observed enhancement in ethanol gas response in Ni-doped CeO_2 sensors is attributed to the reduced grain size of CeO_2, which significantly enhances its ability to adsorb ethanol. This groundbreaking finding offers profound insights for future endeavors aimed at optimizing and enhancing the performance of CeO_2-based ethanol sensors, particularly in critical applications such as gas detection and monitoring.

Acknowledgments

This work was supported by the National Natural Science Foundation of China (No. 51801039), Guizhou Provincial Science and Technology Projects (NO. ZK[2021]242), Sichuan Science and Technology Program (2025ZNSFSC1346).

Conflict of Interest

There is no conflict of interest.

Supporting Information

Applicable.

References

[1] P. Mainkar, A. Ray, S. Chandrasekhar, Solvents: from past to present, *ACS Omega*, 2024, **9**, 7271-7276, doi: 10.1021/acsomega.3c07508.

[2] Y. Herdiana, Alcohol in daily products: health risks, cultural considerations, and economic impacts, *Risk Management and Healthcare Policy*, 2025, **18**, 217-237, doi: 10.2147/RMHP.S495493.

[3] T. Seiyama, A. Kato, K. Fujiishi, M. Nagatani, A new detector for gaseous components using semiconductive thin films, *Analytical Chemistry*, 1962, **34**, 1502-1503, doi: 10.1021/ac60191a001.

[4] L. Zhang, H. Zhang, B. Jiang, ZnO nanostructures fabricated by a two-step hydrothermal method for enhanced ethanol sensing, *Microchemical Journal*, 2025, **209**, 112896, doi: 10.1016/j.microc.2025.112896.

[5] J. Dong, J. Guo, T. Shao, H. Kou, Y. Cheng, F. Zhang, X. Liu, S. Tian, Enhanced ethanol gas sensing performance of Ag/SnO_2 composites, *Sensors and Actuators B: Chemical*, 2025, **423**, 136721, doi: 10.1016/j.snb.2024.136721.

[6] E. Spagnoli, S. Krik, B Fabbri, M. Valt, M. Ardit, A. Gaiardo, L. Vanzetti, M. Della Ciana, V. Cristino, G. Vola, S. Caramori, C. Malagù, V. Guidi, Development and characterization of WO_3 nanoflakes for selective ethanol sensing, *Sensors and Actuators B: Chemical*, 2021, **347**, 130593, doi: 10.1016/j.snb.2021.130593.

[7] T. Montini, M. Melchionna, M. Monai, P. Fornasiero, Fundamentals and catalytic applications of CeO_2-based materials, *Chemical Reviews*, 2016, **116**, 5987-6041, doi: 10.1021/acs.chemrev.5b00603.

[8] Y. Xiao, S. Tan, D. Wang, J. Wu, T. Jia, Q. Liu, Y. Qi, X. Qi, P. He, M. Zhou, CeO_2/$BiOIO_3$ heterojunction with oxygen vacancies and Ce^{4+}/Ce^{3+} redox centers synergistically enhanced photocatalytic removal heavy metal, *Applied Surface Science*, 2020, **530**, 147116, doi: 10.1016/j.apsusc.2020.147116.

[9] D. Dao, T. Nguyena, S. Majhi, G. Adilbish, H. Lee, Y. Yu, I. Lee, Ionic liquid-supported synthesis of CeO_2 nanoparticles and its enhanced ethanol gas sensing properties, *Materials Chemistry and Physics*, 2019, **231**, 1-8, doi: 10.1016/j.matchemphys.2019.03.025.

[10] L. Lyu, Q. Xie, Y. Yang, R. Wang, W. Cen, S. Luo, W. Yang, Y. Gao, Q. Xiao, P. Zou, Y. Yang, A novel CeO_2 hollow-shell sensor constructed for high sensitivity of acetone gas detection, *Applied Surface Science*, 2022, **571**, 151337, doi: 10.1016/j.apsusc.2021.151337.

[11] H. Li, Y. Qu, X. Zhang, The gas sensor utilizing CeO_2 nanorods for the low temperature detection of hydrogen, *Inorganic Chemistry Communications*, 2021, **130**, 108692, doi: 10.1016/j.inoche.2021.108692.

[12] D. Gao, Q. Yu, M. Kebeded, Y. Zhuang, S. Huang, M. Jiao, X. He, Advances in modification of metal and noble metal nanomaterials for metal oxide gas sensors: a review, *Rare Metals*, 2025, **44**, 1443-1496, doi: 10.1007/s12598-024-03027-7.

[13] D. Kuznetsov, B. Han, Y. Yu, R. Rao, J. Hwang, Y. Román-Leshkov, Y. Shao-Horn, Tuning redox transitions via inductive effect in metal oxides and complexes, and implications in oxygen electrocatalysis, *Joule*, 2018, **2**, 225-244, doi: 10.1016/j.joule.2017.11.014.

[14] N. Prabhu, B. Shivamurthy, S. Anandhan, B. Rajendra, S. Kulkarni, Effect of Ni doping on the acetone vapor sensing performance of ZnO nanofibers, *Ceramics International*, 2025, **51**, 730-740, doi: 10.1016/j.ceramint.2024.11.055.

[15] F. Meng, Z. Yu, R. Zhang, H. Gao, Z. Yuan, Study of the Gas Sensing Performance of Ni-Doped Perovskite-Structured $LaFeO_3$

Nanospheres, *Chemosensors*, 2024, **12**, 65, doi: 10.3390/chemosensors12040065.
[16] F. Janene, A. Moulahi, F. Touati, H. Dhaouadi, Gas sensing performance of Ni-doped CuO/ZnO p-n heterostructures for ethanol detection: high sensitivity, selectivity and stability, *Journal of Materials Science*, 2023, **34**, 1800, doi: 10.1007/s10854-023-11224-w.
[17] Z. Dong, Q. Hu, H. Liu, Y. Wu, Z. Ma, Y. Fan, R. Li, J. Xu, X. Wang, 3D flower-like Ni doped CeO_2 based gas sensor for H_2S detection and its sensitive mechanism, *Sensors and Actuators B: Chemical*, 2022, **357**, 131227, doi: 10.1016/j.snb.2021.131227.
[18] A. Verma, B. Yadav, Development and integration of a hierarchical Pd/WO_3 acetone-sensing device for real-time exhaled breath monitoring with disposable face mask, *Journal of Hazardous Materials*, 2024, **463**, 132872, doi: 10.1016/j.jhazmat.2023.132872.
[19] S. Zakaria, S. Samadi, G. Cordshooli, Synthesis and characterization of zirconium (IV) and vanadium (III) doped CeO_2/TiO_2 core/shell nanostructures as a gas sensor, *Sensors and Actuators A: Physical*, 2021, **318**, 112226, doi: 10.1016/j.sna.2020.112226.
[20] M. Thommes, K. Kaneko, A. Neimark, J. Olivier, F. Rodriguez-Reinoso, J. Rouquerol, K. Sing, Physisorption of gases, with special reference to the evaluation of surface area and pore size distribution (IUPAC Technical Report), *Pure and Applied Chemistry*, 2015, **87**, 1051-1069, doi: 10.1515/pac-2014-1117.
[21] Y. Li, Y. Cai, X. Xing, N. Chen, D. Deng, Y. Wang, Catalytic activity for CO oxidation of Cu-CeO_2 composite nanoparticles synthesized by a hydrothermal method, *Analytical Methods*, 2015, **7**, 3238-3245, doi: 10.1039/C5AY00261C.
[22] Z. Dong, Q. Hu, H. Liu, Y. Wu, Z. Ma. Y. Fan, R. Li, J. Xu, X. Wang, 3D flower-like Ni doped CeO_2 based gas sensor for H_2S detection and its sensitive mechanism, *Sensors and Actuators B: Chemical*, 2022, **357**, 131227, doi: 10.1016/j.snb.2021.131227.
[23] G. Ren, L. Wang, S. Wang, Innovative synthesis of CeO_2 nanoparticles for advanced chemical mechanical polishing, *Colloids and Surfaces A*, 2025, **705**, 135764, doi: 10.1016/j.colsurfa.2024.135764.
[24] F. Abbas, T. Jan, J. Iqbal, I. Ahma, M. Naqvi, M. Malik, Facile synthesis of ferromagnetic Ni doped CeO_2 nanoparticles with enhanced anticancer activity, *Applied Surface Science*, 2015, **357**, 931-936, doi: 10.1016/j.apsusc.2015.08.229.
[25] G. Srinet, R. Kumar, V. Sajal, Effects of Ni doping on structural, optical and dielectric properties of ZnO, *Ceramics International*, 2013, **39**, 7557–7561, doi: 10.1016/j.ceramint.2013.03.008.
[26] D. Guruvammal, S. Selvaraj, S. Sundar, Effect of Ni-doping on the structural, optical and magnetic properties of ZnO nanoparticles by solvothermal method, *Journal of Alloys and Compounds*, 2016, **682**, 850-855, doi: 10.1016/j.jallcom.2016.05.038.
[27] U. Holzwarth, N. Gibson, The Scherrer equation versus the 'Debye-Scherrer equation', *Nature Nanotechnology*, 2011, **6**, 534-534, doi: 10.1038/nnano.2011.145.
[28] R. Kostić, S. Aškrabić, Z. Dohčević-Mitrović, Z. Popovic, Low-frequency Raman scattering from CeO_2 nanoparticles, *Applied Physics A*, 2008, **90**, 679-683, doi: 10.1007/s00339-007-4345-6.
[29] S. Colis, A. Bouaine, G. Schmerber, C, Ulhaq-Bouillet, A. Dinia, S. Choua, P. Turek, High-temperature ferromagnetism in Co-doped CeO_2 synthesized by the coprecipitation technique, *Physical Chemistry Chemical Physics*, 2012, **14**, 7256-7263, doi: 10.1039/c2cp23973f.
[30] V. Araujo, W. Avansi, H. de Carvalho, M. Moreira, E. Longo, C. Ribeirod, M. Bernardi, CeO_2 nanoparticles synthesized by a microwave-assisted hydrothermal method: evolution from nanospheres to nanorods, *CrystEngComm*, 2012, **14**, 1150-1154, doi: 10.1039/c1ce06188g.
[31] C. Reddy, I. Reddy, K. Ravindranadh, K. Reddy, D. Kim, J. Shim, Ni-dopant concentration effect of ZrO_2 photocatalyst on photoelectrochemical water splitting and efficient removal of toxic organic pollutants, *Separation and Purification Technology*, 2020, **252**, 117352, doi: 10.1016/j.seppur.2020.117352.
[32] E. Paparazzo, Use and mis-use of x-ray photoemission spectroscopy Ce3d spectra of Ce_2O_3 and CeO_2, *Journal of Physics*, 2018, **30**, 343003, doi: 10.1088/1361-648X/ab5763.
[33] F. Meng, L. Wang, J. Cui, Controllable synthesis and optical properties of nano-CeO_2 via a facile hydrothermal route, *Journal of Alloys and Compounds*, 2013, **556**, 102-108, doi: 10.1016/j.jallcom.2012.12.096.
[34] M. Peck, M. Langell, Comparison of nanoscaled and bulk NiO structural and environmental characteristics by XRD, XAFS, and XPS, *Chemistry of Materials*, 2012, **24**, 4483-4490, doi: 10.1021/cm300739y.
[35] A. Grosvenor, M. Biesinger, R. Smart, N. McIntyre, New interpretations of XPS spectra of nickel metal and oxides, *Surface Science*, 2006, **600**, 1771-1779, doi: 10.1016/j.susc.2006.01.041.
[36] S. Wei, S. Wang, Y. Zhang, M. Zhou, Different morphologies of ZnO and their ethanol sensing property, *Sensors and Actuators B: Chemical*, 2014, **192**, 480-487, doi: 10.1016/j.snb.2013.11.034.
[37] D. Degler, U. Weimar, N. Barsan, Current understanding of the fundamental mechanisms of doped and loaded semiconducting metal-oxide-based gas sensing materials, *ACS Sensors*, 2019, **4**, 2228-2249, doi: 10.1021/acssensors.9b00975.
[38] T. Liu, J. Liu, Q. Hao, Q Liu, X. Jing, H. Zhang, G. Huang, J. Wang, Porous tungsten trioxide nanolamellae with uniform structures for high-performance ethanol sensing, *CrystEngComm*, 2016, **18**, 8411-8418, doi: 10.1039/c6ce01587e.
[39] K. Tao, X. Han, Q. Yin, D. Wang, L. Han, L. Chen, Metal-Organic Frameworks-Derived Porous In_2O_3 Hollow Nanorod for High-Performance Ethanol Gas Sensor, *ChemistrySelect*, 2017, **2**, 10918-10925, doi: 10.1002/slct.201701752.
[40] M. Li, W. Ren, R. Wu, M. Zhang, CeO_2 enhanced ethanol sensing performance in a CdS gas sensor, *Sensors*, 2017, **17**, 1577, doi: 10.3390/s17071577.
[41] G. Hui, M. Zhu, X. Yang, J. Liu, G. Pan, Z. Wang, Highly sensitive ethanol gas sensor based on CeO_2/ZnO binary heterojunction composite, *Materials Letters*, 2020, **278**, 128453,

doi: 10.1016/j.matlet.2020.128453.
[42] Y. Chu, S. Young, Y. Huang, S. Arya, T. Chu, Highly sensitive ethanol gas sensors of Au nanoparticle-adsorbed ZnO nanorod arrays via a photochemical deposition treatment, *ACS Applied Electronic Materials*, 2025, **7**, 2327-2338, doi:10.1021/acsaelm.4c02091.
[43] H. Ding, J. Zhu, J. Jiang, R. Ding, Y. Feng, G. Wei, X. Huang, Preparation and gas-sensing property of ultra-fine NiO/SnO_2 nano-particles, *RSC Advances*, 2012, **2**, 10324-10329, doi: 10.1039/C2RA21121A.
[44] Z. Lin, N. Li, Z. Chen, P. Fu, The effect of Ni doping concentration on the gas sensing properties of Ni doped SnO_2, *Sensors and Actuators B: Chemical*, 2017, **239**, 501-510, doi: 10.1016/j.snb.2016.08.053.